ELEMENTA
Science of the Anthropocene

Doble, MJ, et al 2017 Robust wavebuoys for the marginal ice zone: Experiences from a large persistent array in the Beaufort Sea. *Elem Sci Anth,* X(X): XX, DOI: https://doi.org/10.1525/elementa.233

PRACTICE BRIDGE

Robust wavebuoys for the marginal ice zone: Experiences from a large persistent array in the Beaufort Sea

Martin J. Doble[*], Jeremy P. Wilkinson[†], Lovro Valcic[‡], Jeremy Robst[†], Andrew Tait[†], Mark Preston[†], Jean-Raymond Bidlot[§], Byongjun Hwang[‖], Ted Maksym[¶] and Peter Wadhams[**]

An array of novel directional wavebuoys was designed and deployed into the Beaufort Sea ice cover in March 2014, as part of the Office of Naval Research *Marginal Ice Zone* experiment. The buoys were designed to drift with the ice throughout the year and monitor the expected breakup and retreat of the ice cover, forced by waves travelling into the ice from open water. Buoys were deployed from fast-and-light air-supported ice camps, based out of Sachs Harbour on Canada's Banks Island, and drifted westwards with the sea ice over the course of spring, summer and autumn, as the ice melted, broke up and finally re-froze. The buoys transmitted heave, roll and pitch timeseries at 1 Hz sample frequency over the course of up to eight months, surviving both convergent ice dynamics and significant waves-in-ice events. Twelve of the 19 buoys survived until their batteries were finally exhausted during freeze-up in late October/November. Ice impact was found to have contaminated a significant proportion of the Kalman-filter-derived heave records, and these bad records were removed with reference to raw x/y/z accelerations. The quality of magnetometer-derived buoy headings at the very high magnetic field inclinations close to the magnetic pole was found to be generally acceptable, except in the case of four buoys which had probably suffered rough handling during transport to the ice. In general, these new buoys performed as expected, though vigilance as to the veracity of the output is required

Keywords: sea-ice; waves; Arctic

1. Introduction

The wave buoys described here were designed and built as part of an Office of Naval Research (ONR) Departmental Research Initiative (DRI) focussing on the retreat and breakup of Beaufort Sea ice in summer. The project, called "Marginal Ice Zone" (MIZ), examined the complex and interacting processes by which the continuous pack ice of the early season fractures, melts and retreats to form first the MIZ and then open water (Lee *et al.*, 2014). The project approach centred on a large suite of expendable autonomous drifters (totalling over 70 individual platforms) which were deployed as a North-South array in mid-March from light-and-fast air-supported camps, staged over the course of a week in mid-March. Drifters were grouped in four clusters (numbered 1-4 from South to North) over an approximately 400 km span. The plan was to have each cluster perform a separate ice breakup experiment as the ice edge moved past the instruments.

Once deployed, the drifter array was left to advect with the ice throughout the spring and summer seasons, to be joined in early summer by several autonomous vehicles (Seagliders), deployed from small vessels, which were directed to perform cross-ice-edge transects throughout the open-water season (see other papers in this Special Feature), as well as by SWIFT and WaveGlider wave- and turbulence-measuring platforms (Zippel and Thomson, 2016) near the ice edge.

Scientific results from the wavebuoys are detailed in a number of papers in this Special Feature . The current manuscript focusses on technical aspects of the buoys used as part of the larger MIZ project and is designed to be informative for future development efforts. Many aspects of high-latitude oceanographic equipment are poorly covered in the literature, and several insights were gained from these deployments which will be useful to other groups in this field. The methods section details the physical, electronic and communications design criteria

* Polar Scientific Ltd, Appin, UK
† British Antarctic Survey, Cambridge, UK
‡ Bruncin D.O.O., Zagreb, HR
§ European Centre for Medium Range Weather Forecasting, Reading, UK
‖ Scottish Association for Marine Science, Oban, UK
¶ Woods Hole Oceanographic Institute, US
** Dept. of Applied Maths and Theoretical Physics, University of Cambridge, Cambridge, UK
Corresponding author: Martin Doble (martin@polarscientific.com)

and the chosen solutions. The process of the deployments themselves is discussed, including the important calibration of heading sensors. The results section examines the quality of the directional wave spectra which were the primary scientific aim of the instruments, together with the reliability of the magnetometer-derived heading (and therefore wave direction and spread), which is a constant problem in high-latitude studies. The various phases of the buoys' drifts are identified and discussed, and the survivability and final robustness of the buoys are examined. Actual performance of alkaline battery packs in the Arctic is evaluated. Finally the overall performance of the buoys is evaluated and lessons and improvements for evolution of similar devices in the future are set out.

2. Methods

2.1 Design criteria

Physically, the buoys were designed to cope with all surface conditions to be encountered in the maritime Arctic. They had to be easily transported to the deployment site and straightforwardly installed in a continuous ice cover, have sufficient floatation for open-water episodes, be good surface-followers to give quality directional wave spectra, and provide robust protection for the various on-board systems in challenging wave-ice conditions and convergent ice dynamics. The 24-hour daylight present from their Springtime deployment made solar panels a clear choice as a power source, though these would have to resist riming and freezing spray later in the season, and be significantly over-rated to cope with the usual continuous cloud cover of a maritime Arctic summer. Primary batteries were also required to extend buoy life beyond the light period, as waves were expected until the final winter freeze-up in November. Buoys had to avoid icing build-up which might overturn them, necessitating a stablilising keel and a 'slippery' above-water design.

In addition to these aspects, the buoys needed to be man-handled in-and-out of Twin Otter aircraft with minimum infrastructure – meaning a total weight of less than 150 kg, together with a lack of general awkwardness and no fragile projections to break off or suffer if dropped. The buoys had to be shipped in a state that did not require delicate assembly or manipulation prior to deployment, as the likely surface air temperatures of –35 °C and below in March would preclude bare finger manipulation.

2.2 Final design

All these factors drove us towards a classic keel-stabilised disc layout, with a 1.2 m diameter disk-shaped self-skinning foam surface float. The float was bevelled to allow the buoy to rise up under convergent ice pressure in the time-honoured '*Fram*-like' fashion. The bevel also allowed the assembled buoy to be easily rolled around on the ice for calibration of the three-axis magnetometers. The float surrounded a 10" diameter, 15 mm wall thickness high density polyethylene (HDPE) welded pipe, projecting for 745 mm below the float and 332 mm above. A collar below the float was bolted into place to prevent slippage of the buoy hull through the float if inverted. The pipe contained both alkaline and lead-acid batteries; these latter cells charged by the solar panels, at its base. This positioning both kept the weight low and ensured the batteries were as warm as possible (at the base of the ice) during winter. Both battery packs were nominally 12 V. Battery pack capacities were 56 Ah *Cyclon* lead-acid E-cells (42 cells) and 558 Ah of *Duracell ProCell* alkaline D-cells (248 cells).

Above the float, an HDPE 'deck' mounted three inclined 20 W solar panels, whose charging currents and voltages were independently monitored. The top plate of the pipe (rebated and bolted), providing access to the interior, also mounted the *Iridium* and GPS antennae. The solar panel frame also housed a 640 x 480 pixel webcam (4D Systems uCam II), looking out horizontally in the buoy heading-reference direction and transmitting six-hourly images at 0030, 0630, 1230 and 1830 UTC. The deck, solar panels, webcam, upper pipe and antennae were enclosed by a 5 mm thickness hemispherical Lexan dome, designed to both protect the components from over-riding ice and provide a 'greenhouse' effect against icing and riming, which proved very effective. The dome perhaps also gave some protection from passing polar bears, known for their keen interest in oceanographic instruments. The dome was bolted to the deck with a neoprene gasket to prevent the ingress of water or moisture-laden air. As the assembly was airtight, a pressure-equalisation port was provided, exchanging air through a large-capacity desiccant bottle in order to minimise internal fogging. A magnetic reed switch on the base of the pipe controlled the buoy's activation, by removing a strong magnet acting through the hull/pipe baseplate. **Figure 1** shows a computer-aided design (CAD) drawing of the general arrangement.

2.3 Electronics

The primary scientific sensor was a MEMS-based Attitude and Heading Reference Sensor (AHRS), manufactured by SBG Systems, France. This IG-500-A1G2 unit incorporated three-axis accelerometers (± 2 G), magnetometers and gyroscopes (± 75° sec^{-1}). These nine inputs were sampled at 10 kHz inside the AHRS hardware, before being passed through an anti-aliasing filter of unknown characteristics then optimally combined in a proprietary Kalman filter to provide outputs of heave, roll and tilt at 1 Hz. SBG's "marine" (low dynamics) profile was used to tune the Kalman filter. The magnetometers also provided a heading reference for the buoy, aligned with the pitch (*x)* axis of the orthogonal horizontal accelerometers and co-incident with the webcam view direction. Directional pitch and roll measurements were rotated to Earth co-ordinates in land-based post-processing, using the magnetic declinations calculated at the buoys' positions by the 2013 Defense Meteorological Satellite Program (DMSP-MAG-1) model (Alken *et al.*, 2013).

In a totally quiescent environment, the noise level of the AHRS accelerometers (0.22 mG $Hz^{-1/2}$) coupled with the Kalman filter's interpretation gave a 5 cm peak-to-peak heave signal at a 25 second period. SBG quotes a 10 cm or 10% accuracy for heave. This degree of accuracy was deemed acceptable, since the goal of the project was to

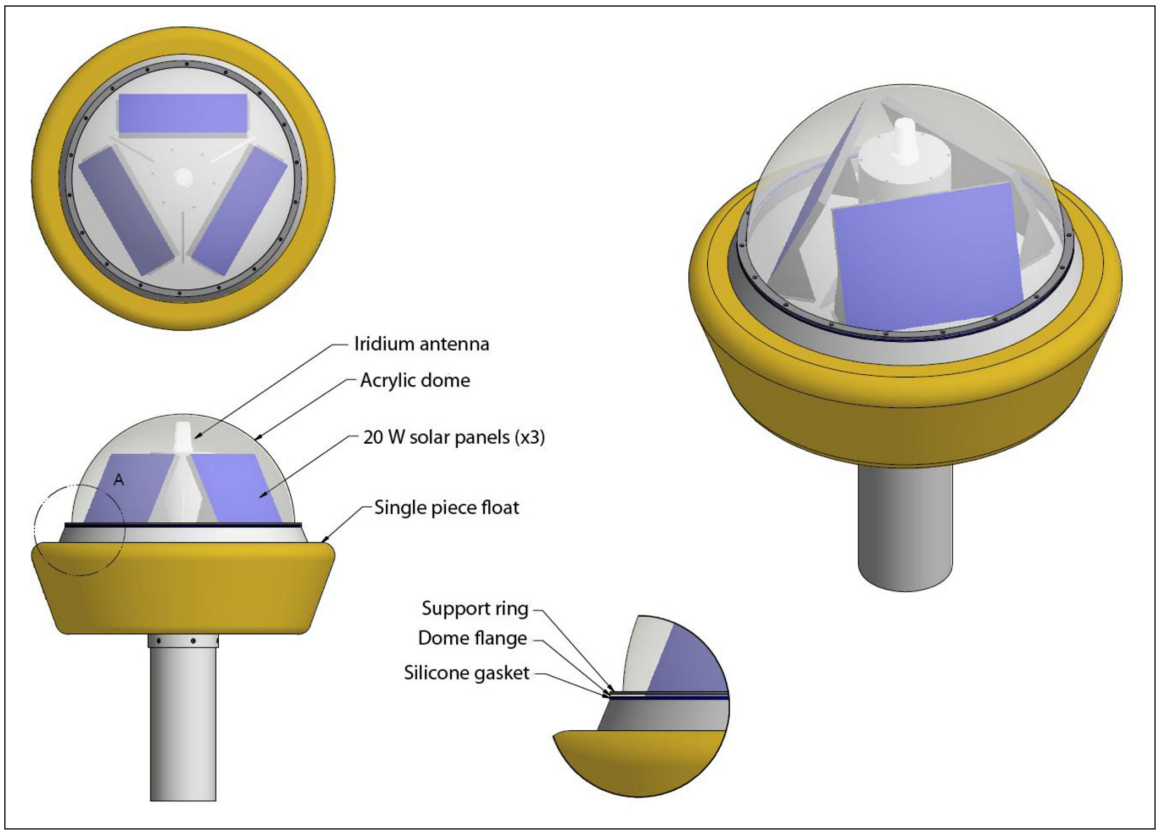

Figure 1: Computer-aided-design drawing of the wavebuoy and main components. DOI: https://doi.org/10.1525/elementa.233.f1

examine ice floe breaking by waves – *i.e.* relatively large-amplitude surface waves – rather than more subtle perturbations for which tiltmeter systems would have been more suited (*e.g.*, Wadhams and Doble, 2009).

Full 1 Hz timeseries of heave, roll and tilt were recorded, together with raw output of *x*, *y* and *z* accelerations (m s^{-2}) to enable the 'black box' Kalman filter-derived outputs to be checked. Heading reference was transmitted at one minute resolution. Other parameters were recorded hourly, on the hour, for transmission. These included GPS position, barometric pressure (using a Freescale Semiconductor MXP-5100-AP sensor), and engineering values – internal temperature and humidity, alkaline and lead-acid battery voltages, 15-minute average CPU load, as well as individual solar panel voltages and charging currents.

Programming and control was performed using an ACME Systems Fox G20 single board computer running a Linux CentOS operating system and programme code developed in C++ and Python. Though the Fox was not the lowest-power device, its ease of use was deemed more important, as the power budget was dominated by the duty cycle of the *Iridium* satellite modem. The Fox controller was mounted to a custom interface board. The board contained; four 10-bit analogue-to-digital converters (monitoring battery voltages and the pressure sensor); two *I2C* connectors, for the solar charge monitoring, power switching controls and the internal temperature/humidity sensor; four serial/TTL ports for the *Iridium* modem, GPS, camera and AHRS. The GPS receiver (SkyTraq S1315R) and temperature/humidity sensors were also mounted on the board, together with all connectors to interface off-board devices.

Data were transmitted over the *Iridium* satellite system using Motorola 9522B modems. These transmitted almost constantly in order to transfer the relatively large quantities of data required: an average of more than 54 kB per hour and a total data throughput of over 3 GB. Modal transmission speed over the entire campaign was 1290 baud, just over half the quoted maximum of 2400 baud. Base level power consumption for the system, without modem operation, was 2.2 W and the average power consumption (including the modem) over the course of a multi-day test was 3.9 W. Though spikes to nearly 12 W during modem operations were evident and frequent, they were extremely short duration and did not overly impact the overall power consumption.

Data transmission was over a custom point-to-point protocol (PPP), developed by Bruncin, with buoys being called in rotation from an array of 13 modems and antennae located at the British Antarctic Survey site in Cambridge. Detailed descriptions and performance metrics of the PPP system can be found in Valcic *et al.* (2014).

Though transmission of timeseries data thus invoked a heavy cost in power terms, the effectively unlimited power availability during long daylight hours makes this decision an easy one. Timeseries data allow for much more flexible analysis of the wave results, as well as enabling further investigation when results look questionable. Several examples of these benefits will be given in forthcoming papers.

2.4 Deployment

Buoys were first staged at the Sachs Harbour airfield, on Canada's Banks Island, having been flown from Yellowknife, Canada, aboard a chartered Buffalo cargo aircraft. The protective wooden packing cases were removed and the buoys separated into float and hull/dome assemblies for loading aboard the Twin Otter aircraft in groups of five (one Twin Otter load per cluster site), using the airfield forklift. Once they had been flown out to the sea ice, unloading the buoys at the cluster nodes without mechanical aid proved relatively simple. Floats and hulls were then re-assembled (a three-man task), before each buoy was flown a short distance by helicopter cargo net to its final deployment site. Buoys were set out in a "five-dice" pattern around the central node at each of the four clusters, an arrangement which maximised utility for small-scale deformation studies using differential kinematic parameters (DKPs) and on a scale (5 km) over which wave attenuation during the eventual ice breakup was expected to be significant.

Each buoy was deployed in level ice, on a slight rise if possible to avoid being completely submerged by large melt-ponds, relatively far from ridges and deformed features which would complicate the heave response of the buoy during breakup. A 10-inch hole was drilled with a petrol-driven auger to approximately one metre depth, sufficient to prevent the hull tube from reaching the bottom.

Power was then applied to the buoy, *via* the internal magnetic switch. Following boot up, the buoy performed a 10-minute electronic warm-up, then entered the calibration routine. Buoy status was indicated throughout by a bright, sunlight-readable LED, flashing at defined intervals. A 3D magnetic calibration was performed: the buoy was held vertically upright and spun in the vertical axis; the buoy was then laid down, held horizontal and spun slowly in a horizontal axis; finally the buoy was lain on the ice and rolled around a complete horizontal circle. Given the weight and size of the unit, this approach was thought to be the best that could be achieved in the field.

Once the status LED indicated successful completion of the calibration phase, the buoy was then manoeuvred into the pre-drilled 10-inch hole, with the float bottom resting on – and approximately parallel to – the snow surface. Precise levelling was not required, since the AHRS uses the three accelerometer axes to determine vertical heave at any inclination angle. No ablation shield was placed under the float, as is sometimes done for ice buoys, because the buoy was designed to float free when the larger ice cover melted or broke out, though the white finish of the float was designed to minimise local heating effects.

The wavebuoys were co-located with ice mass-balance buoys (IMBs), with the wavebuoy's webcam directed at the IMB or automatic weather station (if present) to gain understanding of surface conditions, particularly during the melt-ponding phase, and any problems with those instruments. If possible, it was also arranged for the webcam to point South, in order to minimise icing of the dome in front of the camera.

In total, 19 of the 20 wavebuoys were successfully deployed. Problems were encountered with one unit (208) which failed to boot up on the ice and which the imminent final departure of the aircraft did not allow time to resolve. Characteristics of each deployment site are given in **Table 1**. Ice type (first year or multi-year) was largely determined *post-hoc* using precisely-geolocated satellite (TerraSAR-X) images, as conditions on the ground were less clear-cut without sufficient time for ice coring and subsequent salinity analysis. Initial ice thickness was taken from drilling during installation of the IMBs, as well as from their transmitted data.

3. Results

3.1 Character of the drifts

Four clear divisions in the lifetime of the buoys can be observed, and are plotted in terms of the inclination of buoys in each of the four Clusters, in **Figure 2**; deployment phases for all 19 buoys are summarised in **Figure 3**:

1. *Quiescence*: The first 100 days of the buoys' deployments (until the beginning of June) were uneventful, as they advected westwards with little relative movement or deformation within the Clusters. Webcam images show dominantly clear-sky conditions, interspersed with occasional icing events during the colder hours. Surface conditions show little evolution. WB220 is the exception, as its ice floe was broken on 21 May. Its webcam images showed repeated convergent/ridging events until it was finally released on 5 September. Only one buoy (WB203) failed to survive this phase.
2. *Melt*: The sudden onset of melt ponding is observed quasi-simultaneously by all webcams, in mid-June (as also observed in remote sensing images – see Hwang et al., 2017, in this Special Feature). Melt water very rapidly covers an appreciable fraction of the view (within one to two days). The melt of the snow cover removes the support from beneath the wavebuoy floats, and they topple onto their sides – at inclinations up to 70° – immediately or shortly afterwards, as indicated by the short or absent magenta sections (time between melt onset and toppling) in **Figure 3**. Inclinations less than 70° suggest that the hull tube is still partially supported in the remaining ice hole depth, as was the case for WB212 which was visited by the USCG *Healy* on 20 August (inset, **Figure 2**). The co-incidence of the melt onset across all clusters is striking, though by this time the buoy array had undergone a marked clockwise rotation in the first week of June, from a dominantly North-South alignment before, to a dominantly East-West one afterwards. Buoys were therefore all at a similar latitude at the time of melt onset.
3. *Release*: The buoys are suddenly restored to an upright position when the ice floe around them either melts completely or breaks up, releasing

Table 1: Summary of the wavebuoy deployments. DOI: https://doi.org/10.1525/elementa.233.t1

Cluster	WB No.	Deployed[a]	Ice type[b]/ thickness[c]	MP onset, falls over	Floats	End solar charging, refreezes	Last message [d]	Co-located assets[e]
1 – node	**210**	16 Mar	FY, 1.52 m	18 Jun, 2 Jul	18 Aug	27 Aug, NA	6 Sep (ridged)	IMB07, AWS01
1 – NW	**219**	17 Mar	MY, 2.45 m	21 Jun, 25 Jun	16 Aug	ND, NA	6 Sep (ridged)	IMB15
1 – NE	**203**	16 Mar	FY?, 1.6 m	NA	NA	NA	11 May	IMB18
1 – SE	**216**	16 Mar	MY, 3.62 m	22 Jun, 25 Jun	NA	18 Aug, NA	22 Aug	IMB13
1 – SW	**207**	16 Mar	MY, 1.40 m	19 Jun, 8 Jul	22 Aug	16 Aug, 18 Sep	**19 Oct**	IMB12
2 – node	**211**	14 Mar	MY, 1.74 m	22 Jun, 24 Jun	18 Aug	22 Aug, 5 Oct	**30 Oct**	IMB17, AWS02, IS01
2 – NW	**212**	15 Mar	MY, 1.98 m	20 Jun, 2 Jul	21 Aug	1 Sep, 14 Oct	**4 Nov**	IMB06
2 – NE	**214**	17 Mar	MY, 1.70 m	22 Jun, 22 Jun	23 Aug	ND, 21 Sep	**20 Oct**	IMB10
2 – SE	**215**	17 Mar	MY, 1.86 m	22 Jun, 2 Jul	28 Aug	18 Aug, 6 Oct	**27 Oct**	IMB03
2 – SW	**201**	17 Mar	MY, 1.84 m	22 Jun, 25 Jun	26 Aug	1 Sep, 29 Sep	**1 Nov**	IMB02
3 – node	**208**	DOA	FY, 1.38 m	DOA	DOA	DOA	DOA	IMB04, AWS03, IS02
3 – NW	**206**	19 Mar	MY, 3.41 m	22 Jun, 14 Jun	14 Sep	1 Sep, 6 Oct	**25 Oct**	IMB19
3 – NE	**213**	19 Mar	FY, 1.53 m	22 Jun, 22 Jun	29 Jul	18 Aug, 7 Oct	**27 Oct**	IMB11
3 – SE	**202**	19 Mar	MY, 1.62 m	22 Jun, 27 Jun	13 Aug	1 Sep, 17 Oct	**26 Oct**	IMB16
3 – SW	**218**	20 Mar	MY, 3.75 m	22 Jun, 22 Jun	NA	NA, NA	8 Jul	IMB08
4 – node	**209**	20 Mar	FY, 1.49 m	22 Jun, 24 Jun	27 Aug	1 Sep, 17 Sep	3 Oct	AWS04, IMB09
4 – NW	**220**	20 Mar	MY, 1.65 m	ND	5 Sep	ND, 9 Sep	**25 Oct**	IMB05
4 – NE	**204**	20 Mar	MY, 1.80 m	22 Jun, 24 Jun	16 Aug	28 Aug, 26 Sep	**14 Oct**	IMB14
4 – SE	**217**	20 Mar	MY, 1.64 m	22 Jun, 5 Jul	2 Sep	ND, 8 Oct	**24 Oct**	IMB20
4 – SW	**205**	21 Mar	MY, 1.78 m	22 Jun, 17 Jun	NA	NA	29 Jul	IMB01

[a] Dates are all based on UTC timings. DOA = dead on arrival (buoy did not boot up). ND = no data; NA = not applicable (buoy did not survive to this stage).
[b] Ice type is derived from synthetic aperture radar (SAR) backscatter from the TerraSAR-X satellites and observations at deployment. FY = first year ice; MY = multi-year ice.
[c] Initial ice thickness (excluding snow thickness) is from ice mass balance buoy data and drilling during deployment.
[d] Last transmission dates in bold indicate that the buoy continued functioning until its battery pack was exhausted.
[E] Co-located assets are ice mass-balance buoys (IMBs), automatic weather stations (AWS) and ice/snow buoys (IS).

them to float freely. Though more dispersed in time than the melt onset, release was confined to a short period across Clusters 1 and 2 (16 to 26 August), with more variation observed in Clusters 3 and 4. Buoy inclinations become noisy during this floating period, as the buoys responded to waves and were periodically gripped in convergent events at varying inclinations. Many of the buoys survived repeated convergent events, giving close-up views of large ice blocks in many webcam images, and suggesting that the dome design for survivability was a good one.

4. *Freeze-up*: The inclination of the buoys return to a quiescent state as they are re-incorporated by the advancing winter pack ice, far from the influence of open water waves. Buoys refroze at various inclination angles, depending whether they were caught by convergent ice conditions, and finally ceased transmissions once their primary alkaline cells were exhausted.

3.2 Cause of eventual failure

Battery life

Twelve of the 19 buoys functioned until the exhaustion of their alkaline battery packs, indicated by bold type for the last transmission dates in **Table 1**. **Figure 4** shows battery voltages for one such buoy, where WB201 was solar-powered until year-day 245 (1 September), at which point the lead acid voltage dropped below the alkaline pack and the primary batteries were used until their exhaustion on year-day 305 (1 November), when the voltage dropped towards 9V. The slight positive gradient in alkaline voltage early in the record is due to increasing internal temperature as the summer progressed. Increased charging early in the record compared with later for a given solar elevation angle is due to the cold and clear-sky conditions in Spring, compared to the much cloudier conditions prevalent in the more open ice of the autumn.

It is common to down-rate alkaline cells by 50% to account for the low temperatures encountered in Arctic deployments, but the observed duration of the alkaline

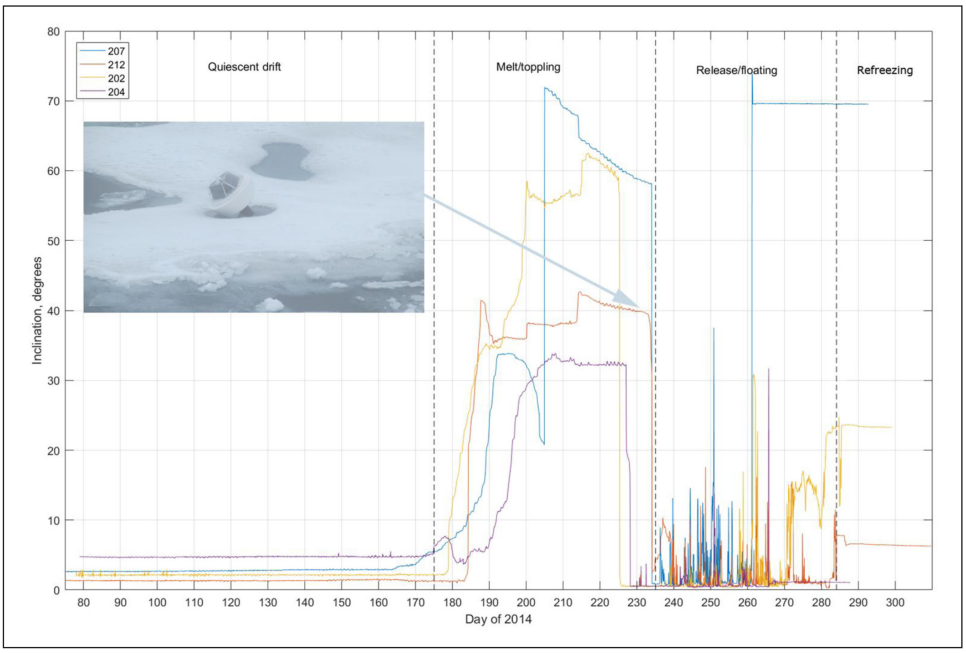

Figure 2: Inclination of buoys in each of the four clusters over their lifetimes. Vertical dashed lines separate the four phases of buoy life: quiescent drift, melt/toppling (snow melt onset leading to loss of support and toppling), release/floating (vertical floating during which waves are observed), and refreezing (indicated for various inclination angles). Inclination plotted is the root sum square of the *x* and *y* tilts. The inset photograph (credit R. Hanson) shows buoy 212 on August 20 2014, when it was encountered by the USCG *Healy*. The arrow indicates the time and inclination reported by the sensors; tt broke out and began floating two days afterwards. DOI: https://doi.org/10.1525/elementa.233.f2

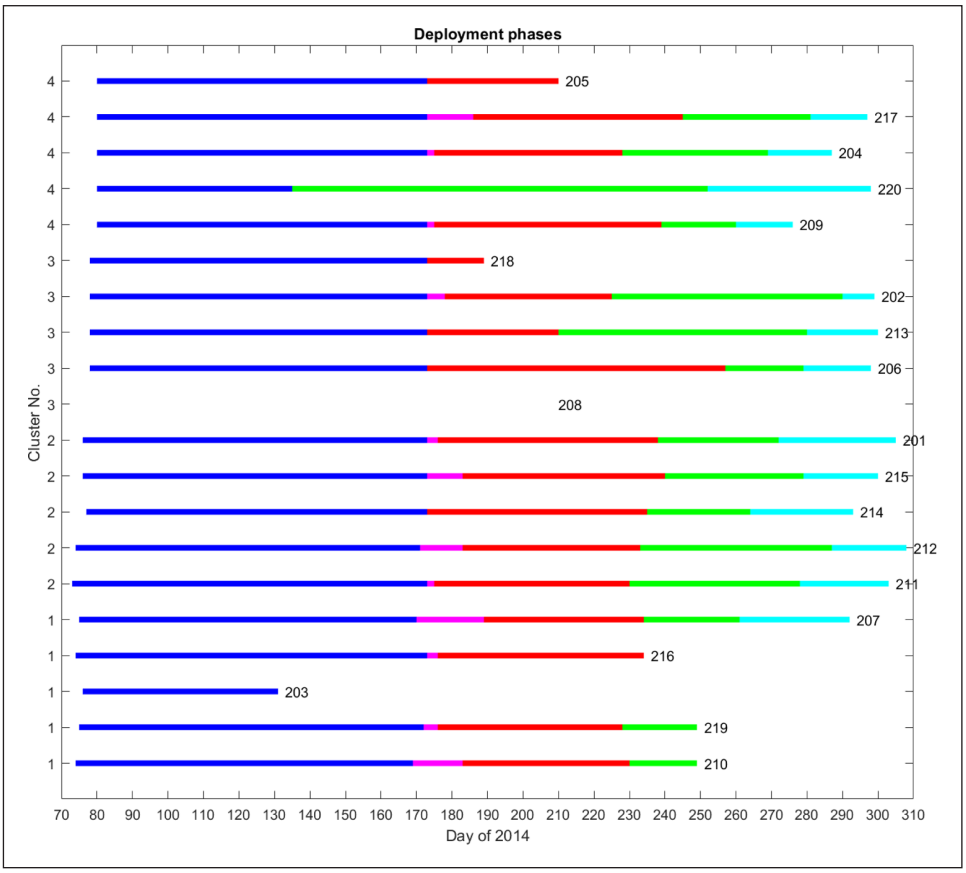

Figure 3: Timeline of the four phases for all buoys, arranged by cluster. Phases are indicated by colour: blue fpr quiescence; magenta formelt onset to buoy toppling, if later; red formelt (buoy toppled); green forrelease/floating; cyan for refreezing. Buoys are arranged by cluster, from Cluster 1 in the south to Cluster 4 in the north. DOI: https://doi.org/10.1525/elementa.233.f3

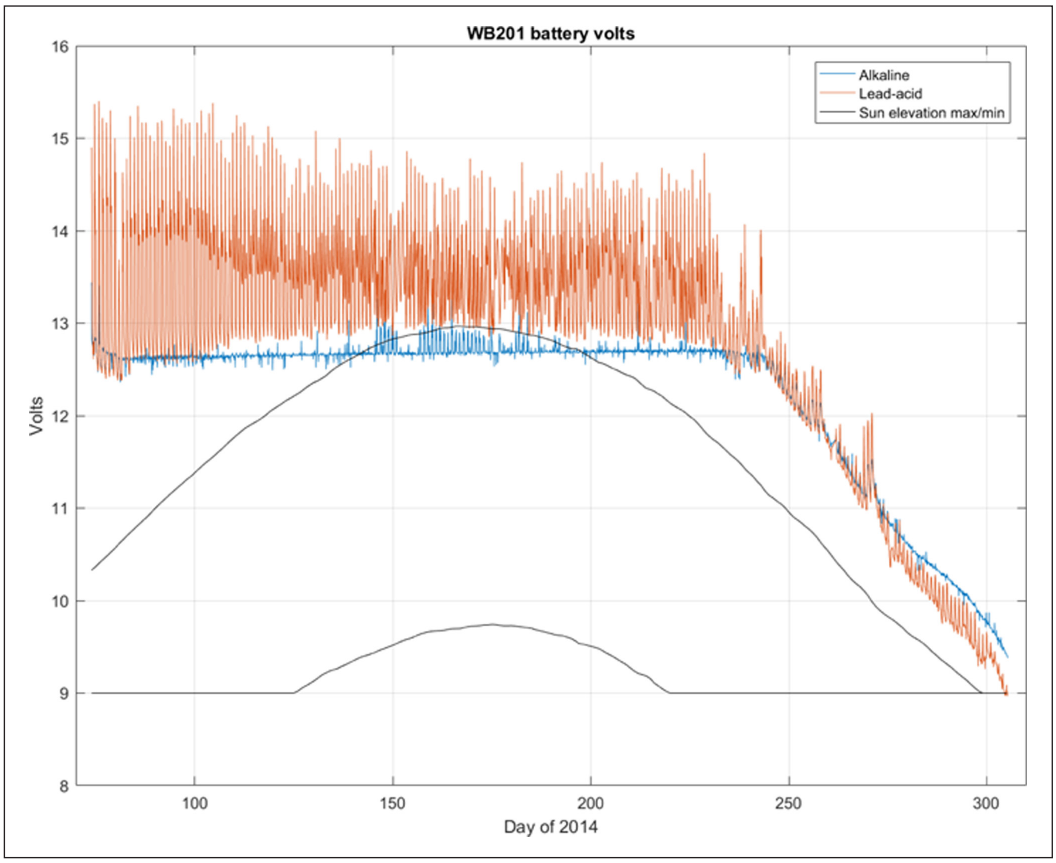

Figure 4: Alkaline and lead acid battery voltages throughout the life of WB201. The solar panels could not sustain the lead-acid battery voltage (red line) past 1 September, at which point the primary alkaline batteries (blue line) begin to supply power, finally reaching exhaustion on 1st November. The black curves shows the daily maximum and minimum solar elevation angles (scaled to fit; sun angle reaches a maximum of 40° at the buoy›s location). Wobbles in the solar elevation are due to latitudinal variations in the buoy›s position. DOI: https://doi.org/10.1525/elementa.233.f4

packssuggests that this down-rating is over-conservative. If all of the energy in the 12 V/558 Ah packs were available for use, the measured 3.9 W average power consumption would exhaust the batteries in (558*12)/(3.9*24) = 70 days. Three of the wavebuoys (WB211, 213 and 215) in fact achieved 71 day autonomy with the alkaline packs, and three others achieved 62 to 65 days, though the power remaining in the 56 Ah lead-acid cells also contributes here. This degree of autonomy suggests that no real down-rating is required under these conditions. Of course, the hulls containing the batteries are surrounded by seawater at −1.8 °C, and the power dissipation of the buoys will further raise the internal temperature by several degrees. It is nonetheless interesting to note that apparently the whole quoted energy can be used in these applications.

Ice convergence

In other cases, the solar panels were still charging strongly when the buoy ceased transmission, suggesting an ice-mechanics-induced failure through ridging. In these cases, a buoy may either have been crushed or simply buried under ice rubble and unable to transmit. This failure mode is particularly indicated when two adjacent buoys went silent simultaneously, as was the case for WB210 and WB219 in the southern-most Cluster 1. WB219 offers the clearest evidence from this source, with the final two webcam images (**Figure 5**) being extreme close-ups of an ice ridge. WB210 images suggest a similar cause. WB209 appeared to have survived freeze-up surrounded by loose ice fragments, though such a matrix of thick and thin ice is dangerous under convergence, rapidly forming rubble fields or ridges. DKPs do not show any significant convergence to have occurred just prior to its failure, however.

The earliest buoys to fail (WB203, 205, 216, 218) give little clue from their webcam images as to the cause of premature failure, showing them still in their original undeformed floe, without any visible recent change prior to their silence. The six-hour interval leaves ample time for dynamical changes between images, however. For WB216, we can infer dynamics as the cause since its neighbour (WB207) is released at the same time and local DKPs show cyclical convergence/divergence for two days prior to failure. WB216 was unique for these deployments as it was installed in a massively thick (3.6 m) multi-year floe which would have presented a formidable challenge when broken and combined with convergent dynamics. DKPs for WB205 and its neighbours show eight days of divergence followed by eight days of convergence before the end of transmissions from WB205, so this was likely ridged/crushed. WB218 showed no significant dynamic behaviour and transmitted valid GPS fixes until it went silent.

GPS failure

Figure 6 shows the number of daily valid GPS fixes for each buoy, with green indicating the full complement of 24 daily fixes. While 14 of the buoys maintained close to 100% GPS performance throughout, five buoys stand out in this analysis: WB203 struggled to maintain good GPS performance from the beginning of its record, then sent 13 days of invalid GPS fixes before going silent, though

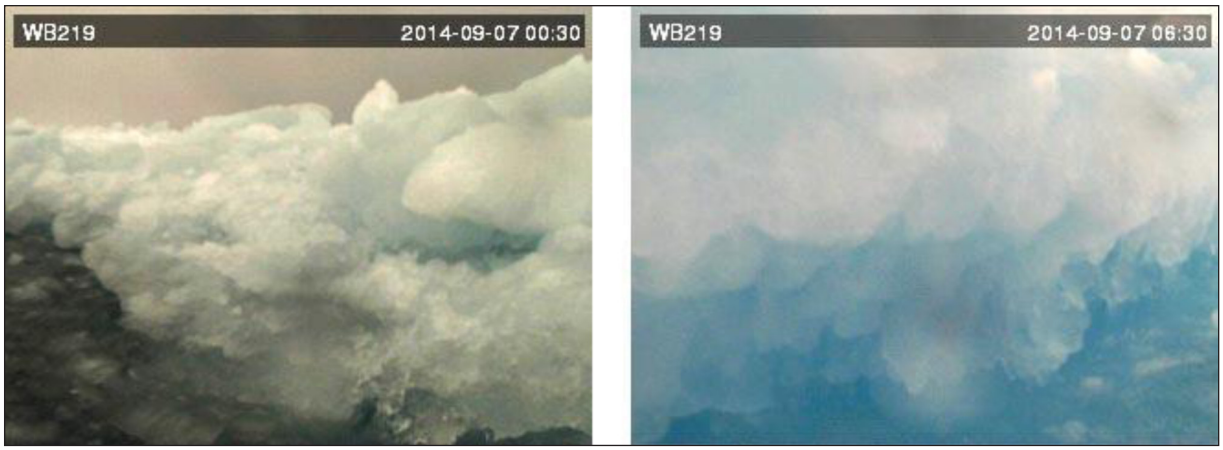

Figure 5: The final webcam images from WB219. Images show the over-riding of the buoy by deformed ice just before transmissions ceased. DOI: https://doi.org/10.1525/elementa.233.f5

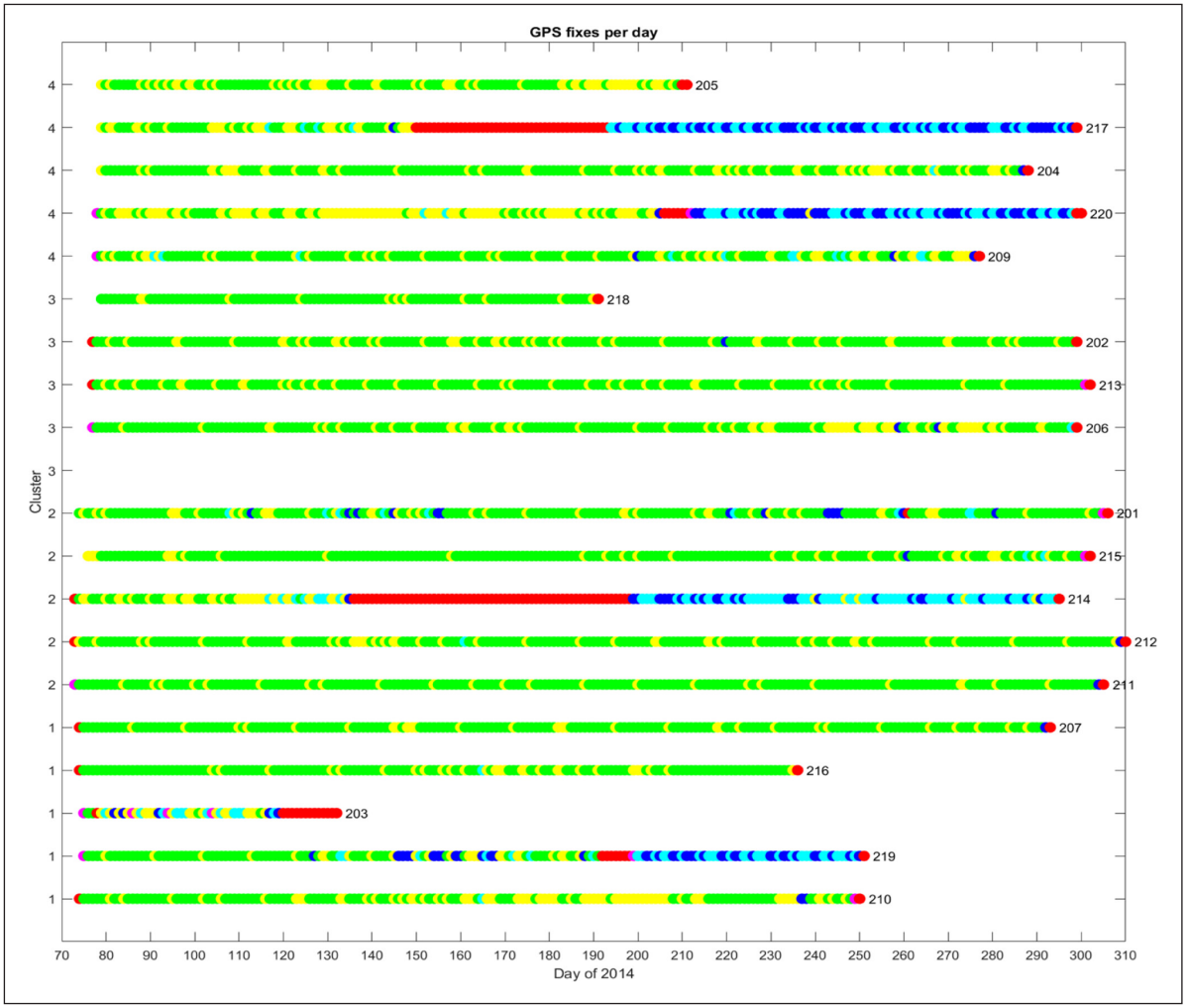

Figure 6: The number of daily valid GPS fixes transmitted by each buoy. The colour scheme indicates the number of valid fixes received each day from each buoy (buoy number indicated to the right of each colour bar), as follows: green: 24 (100%); yellow: 22–23; cyan: 20–21; blue: 10–19; magenta: 5–9; red: 0–4. Buoys are arranged by cluster, from Cluster 1 in the south to Cluster 4 in the north. DOI: https://doi.org/10.1525/elementa.233.f6

its webcam maintained a clear view throughout. WB214 and WB217 had long periods (62 and 41 days respectively) without any valid GPS fixes. WB219 and WB220 also had periods without valid fixes, though these were of much shorter duration, at around six days each. These drop-outs were eventually identified as being due to software failures in the GPS receiver chips. Using the *Iridium* two-way communication protocol, we were then able to remotely log into the buoy controllers and soft-reboot the GPS chips, which partially solved the problem. None of the four systems ever recovered 100% reliability, but all were able to maintain around 20 fixes-per-day (down from 24) from then on. Though unfortunate, the episodes did show the advantage of having total remote two-way access to the buoy systems over the satellite link.

Spring reboot

The one serious disappointment encountered was that none of the buoys booted up again the following Spring, when we might have expected the solar panels to have re-activated any surviving buoys. Given the demonstrated robustness of the buoys to ridging, it seems unlikely that all 12 surviving members were mechanically destroyed over Winter. Few precautions were taken in the design to prevent deep discharge of the lead-acid cells, however, and it seems most likely that these Cyclon cells were unable to accept sufficient charge the following Spring to re-activate the buoys. Following this experience, subsequent designs have been modified to leave the solar-charging batteries fully charged over winter.

Significant problems were encountered with the *Iridium* PPP connection towards the end of 2014 and into the following year (though RUDICS connections apparently remained unaffected), so it is also possible that some units were actually alive but that we were unable to contact them.

3.3 Wave data quality control

The advantage of having timeseries data was clearly demonstrated when examining the heave records of several buoys. Plotting the heave timeseries suggested that occasional significant wave events were occurring which were short-duration, highly episodic and with very rapid onset and cessation. These events were unrelated between closely-spaced buoys and were thus not consistent with our understanding of wave propagation in ice.

Closer examination of the raw vertical (*z* axis) acceleration timeseries revealed problems with the outputs at these times. While normal motion showed the expected sinusoidal, slowly varying z-acceleration, these abnormal episodic events had a saw-tooth character, slewing between extreme positive and negative values in successive 1 Hz samples. The heave signal, calculated by the 'black box' Kalman filter to make sense of its inputs and constrained by its programming to provide a "marine-like" output, becomes totally unrepresentative of what is actually happening. We postulate that the events seen in the raw accelerations are due to ice impact on the wavebuoy, as it moves with significant waves in close proximity to ice fragments. The ± 2 G accelerometers (chosen for their sensitivity in the generally low-amplitude wave field) are saturated by the transient accelerations imparted by the impacts.

Data output from the Kalman filter during these events are thus misleading and must be flagged as invalid. Existing check factors – developed for open-ocean buoys – often perform poorly in the context of ice, however. These check factors typically compare the horizontal and vertical displacements (*e.g.*, Thomson *et al.*, 2015), a ratio which should be close to one for the orbital motion of open water waves (Mei, 1989). The presence of ice can severely constrain horizontal motion if the ice feature is larger than the dominant wavelength, leading to unnecessary removal of good records. Other quality control methods compare the wavenumber derived from cross- and auto-spectra (k_d, as detailed in Appendix A of Kuik *et al.*, 1988) to that (k_t) given by the open water dispersion relation (*e.g.*, Long, 1980). Again we find this approach to be problematic for buoys embedded in an ice cover, as wavenumber in the swell band can deviate significantly from the open ocean values.

The *z*-acceleration was therefore used to reconstruct the displacement timeseries without the influence of the Kalman filter, using a time-domain moving-average filter. This filter was designed in the frequency domain to achieve the required multiplication by $-1/w^2$ and also incorporated a high-pass filter to remove low-frequency drifts which result from simple integration acting on low-frequency noise (Tucker, 1991). Earlier buoy deployments, such as those discussed in Doble and Bidlot (2013), used a similar scheme to derive the one-dimensional spectra from vertical accelerations.

Comparing the RMS values of the Kalman-output heave and the double-integrated *z*-acceleration over 30 minute periods showed the ratio between these displacements to give good discrimination of impact-contaminated data. During valid periods, the ratio of RMS values is close to unity and this rises to over 20 during impact events. A ratio threshold of 5 was empirically found to be the best threshold for these instruments.

3.4 Heading quality

When dealing with directional parameters, operations close to the magnetic pole often give cause for concern. The proximity to the Pole results in small horizontal field components which make the task of determining magnetic north more difficult than usual. Manufacturers usually specify a magnetic field inclination limit for reliable headings – SBG state 80° field inclination as the limit for the IG-500A used in this study, for example – whereas Arctic deployments often exceed this criterion. For the current study, field inclinations were typically 83 to84° and problems in heading accuracy might be expected as a result. This limitation can be overcome using GPS-based compasses, which exploit the phase difference across two closely-spaced (< 30 cm) antennae to give reliable headings at any point on the globe. These devices are currently too power-hungry for extended autonomous applications however, being designed for installation in survey vessels and similar platforms. Several buoys do now incorporate

these heading sensors, such as the SATICE buoys (Elosegui *et al.* 2012) and the O-buoy series (Knepp *et al.*, 2010). These designs opted for massive lead-acid battery banks charged from very large solar panels which are unsuitable in this application, so we must accept the sub-optimal solution of magnetometer-based headings in the far north in this context, at least at present.

An evaluation of the heading error caused by exceeding the field inclination specification would be very useful in this context and cannot easily be found in the existing literature. We therefore examine the rich wavebuoy dataset to determine the heading quality in five independent ways, looking at the usefulness of each method.

3.4.1. Comparison with WAM mean wave direction

We first compared the dominant wave arrival directions measured by the buoys for consistency with an operational wave model (WAM, provided by the European Centre for Medium Range Weather Forecasting, ECMWF). It should be noted that the operational WAM does not 'see' the low concentration ice present during the wave events, as it uses OSISAF passive microwave ice concentrations, derived from the AMSR2 satellites, as an ice mask. WAM thus allows waves to grow and propagate across the region as if it were open water, though the directions should be broadly correct.

Comparisons with WAM show much greater variability of the buoy-derived principal wave directions. This greater variability is expected, since the buoys will be influenced by local ice and wave conditions, as well as by uncertainties in the directional solution during relatively low-amplitude wave conditions. Comparisons are limited to times when the buoy-derived SWH exceeds 7 cm – such that the AHRSs have a reasonable signal to work with – and contamination by ice impact, as discussed in the previous section, is not indicated. With these provisos, the directional comparison appears reasonable. While there is considerable scatter, the wave directions are generally grouped close to the WAM results, with no significant bias in any direction. We summarise results for all buoys that experienced significant waves as an RMS directional error and bias, together with the number of instances concerned, in **Table 2**: RMS heading difference varies between 33° and 56°, while any bias either side of the WAM result is mostly in single figures. Only nine of the 19 buoys (those that experienced significant waves) can be assessed in this manner, however, and we must look to other methods to constrain the rest.

3.4.2. Heading versus bearing

Additional information of heading reliability can be gained from examining the rotation of a single Cluster, with closely-spaced buoys, before the ice cover within that Cluster experienced significant differential deformation. In such a scenario, the change in heading with time for each individual buoy should match the change in bearing between buoy pairs (derived from GPS positions, thus independent of the headings). The test only serves to validate a buoy's heading in the positive sense however; any discrepancy between a buoy's heading and the rotation of its position may be due to small-scale motion local to the buoy's floe.

Figure 7 shows the results for buoys of Cluster 2, plotting only four buoy-to-buoy bearings for clarity (bottom panel; there are a total of 10 bearings between five buoys). All buoy-to-buoy bearings change in a similar manner, rotating by approximately 40° by the end of the period shown, and validating the assumption of no deformation. Headings from buoys 211, 212 and 214 (top panel) track these bearing changes closely, also reaching approximately 40° change by the end of the period. Buoy 201 and 215 headings change much less, however, only reaching 25° and 15° change respectively. As already mentioned, while these results give confidence in the first three buoys, 201 and 215 may be valid if their ice floes were under-rotating for local reasons. All buoys show some diurnal variation in heading, typically resulting from inertial oscillations. This effect is particularly marked for 212, which varies by more than 20°. In other Clusters, buoys 203, 204, 210 and 220 show similar amplitude oscillations.

The "HvB" column of **Table 2** indicates buoys whose heading changes closely match buoy-to-buoy bearing changes within its Cluster ("Y"). If the buoy's heading significantly under-represents the bearing changes, this effect is noted by comparing the heading/bearing change values. A few buoys cannot be assessed, either due to their early demise (203) before any significant rotation took place or local deformation prior to any significant rotation (particularly Cluster 3); these are marked "NA", not available, in the table.

3.4.3. Lifetime heading range

Buoys are expected to experience considerable rotation during their lifetimes, and any buoy having a limited range of headings over this period may indicate problems. This test is indicated in the "360?" column of **Table 2**. One buoy (213) shows almost no variation in heading throughout its lifetime, and its heading can be considered bad. If buoys do not display the full 360° variation during their lifetime, the range of headings experienced is given. Other than 213, four buoys (206, 214, 217, 218) did not display the full range of possible headings . It is possible that they did not actually undergo a full rotation at any time, however. As three of these four are in the deformed Cluster 3, that may be the case, but further confirmation is still required.

3.4.4. Solar azimuth

For an absolute test of the heading accuracy which can identify both good and bad headings, the six-hourly webcam images again demonstrated their usefulness. Solar azimuth – the angle of the sun projected onto the horizon from geographic North - can be directly observed in the images and compared with a precise calculated figure, knowing the time, date, position and altitude of the observer.

Each buoy's webcam is aligned with its heading direction, thus knowing the horizontal field-of-view of the camera (56°) gives the observed solar azimuth as the sum of the relative solar azimuth in the webcam image (positive

Table 2: Validation of buoy heading quality by comparison with WAM, heading versus bearing, total variation and solar azimuth. DOI: https://doi.org/10.1525/elementa.233.t2

Cluster	ID	Npts [a]	RMS (WB − WAM) [b]	Bias [c]	HvB [d]	360? [e]	Sun Az [f]	Deployed heading [g]
1	**210**				Y	Y	10°,2	Y
1	**219**				Y	Y	17°, 1	Y
1	**203**				NA	Y	NA	Y
1	**216**				Y	Y	9°,3	Y
1	**207**	90	40°	−9°	NA	Y	10°, 6	Y
2	**211**	134	33°	+9°	Y	Y	18°, 11	Y
2	**212**	212	38°	+7°	Y	Y	21°, 7	Y
2	**214**	59	43°	−5°	Y	120–350°	25°, 2	Y
2	**215**	133	50°	0°	15/40	Y	32°, 2	N
2	**201**	86	33°	+4°	25/40	Y	14°, 5	Y
3	**206**	337	56°	+7°	NA	50–100°	122°, 7	N
3	**213**	225	49°	+4°	bad	280–340°	195°, 10	N
3	**202**	235	56°	+13°	NA	Y	55°, 8	Y
3	**218**				NA	150–350°	15°, 5	Y
4	**209**				Y	Y	14°, 6	Y
4	**220**				Y	Y	11°, 5	Y
4	**204**				Y	Y	9°, 11	Y
4	**217**				5/28	20–144°	87°, 3	N
4	**205**				Y	Y	21°, 3	Y

[a] "*Npts*" is the number of 30-minute wave segments considered.
[b] For the WAM comparisons, only buoys with a reasonable number of valid wave directions are tabulated: ; "*RMS*" is the root-mean-square error between buoy- and WAM-derived wave directions.
[c] "*bias*" is the sum of the (signed) errors, divided by *npts.*
[d] The Heading-*versus*-Bearing (HvB) test was performed on all buoys, '*Y*' indicating that the buoy rotation closely matched overall rotation of the Cluster. Figures in this column show the total rotation of the heading/rotation of the bearing during the undeformed period examined, if the buoy is seen to under-rotate significantly. NA indicates that early deformation or cessation of transmissions precludes a reasonable assessment.
[e] The "360?" column indicates if the buoy heading varies over the complete 360° range of possibilities, and indicates the limited range if not.
[f] The "Sun Az" column indicates the mean deviation (degrees) of the sun azimuth calculated from the webcam images from the correct celestial figure, together with the number of webcam images on which the assessment was based (total 97).
[g] The "Deployed heading" column indicated whether the mean heading over the first few days of deployment agrees with the expected orientation.

to the right of centre in the image) and the True buoy heading. For these purposes, the buoy heading is taken as a 10-minute average centred on the image time, and images when the heading is changing very rapidly or the horizon is significantly inclined are discarded. The number of observations is limited, as the solar disc must be clearly defined in the image (such as in the inset webcam image in **Figure 8)** and the field-of-view is relatively narrow. Six-hourly images 'catch' very few direct observations as a result, and the sun in these images can be obscured by cloud (most commonly), fog or icing of the dome, the sun may be too high in the sky (out of the vertical field of view), or, during the toppled period, the camera may be pointing down at the ice floe.

Nonetheless, we were able to identify 97 images across 18 buoys (203 excepted) for which reliable solar azimuths could be measured, and these are plotted against the calculated figures as a scatter plot in **Figure 8**. The nine buoys which were identified as 'good' in both *HvB* and *360* tests are plotted as solid coloured circles, while buoys which may have failed one or more previous tests are plotted as open circles. Since images were taken at four discrete times, the calculated solar azimuths (*y*-axis) plot in four discrete groups, and their UTC and local times are indicated. Local time is approximately nine hours behind UTC. The mean (unsigned) difference between the expected and observed azimuths, *da*, (**Table 2**) gives a quantitative measure of success, with 25° mean deviation suggested as a quality flag threshold.

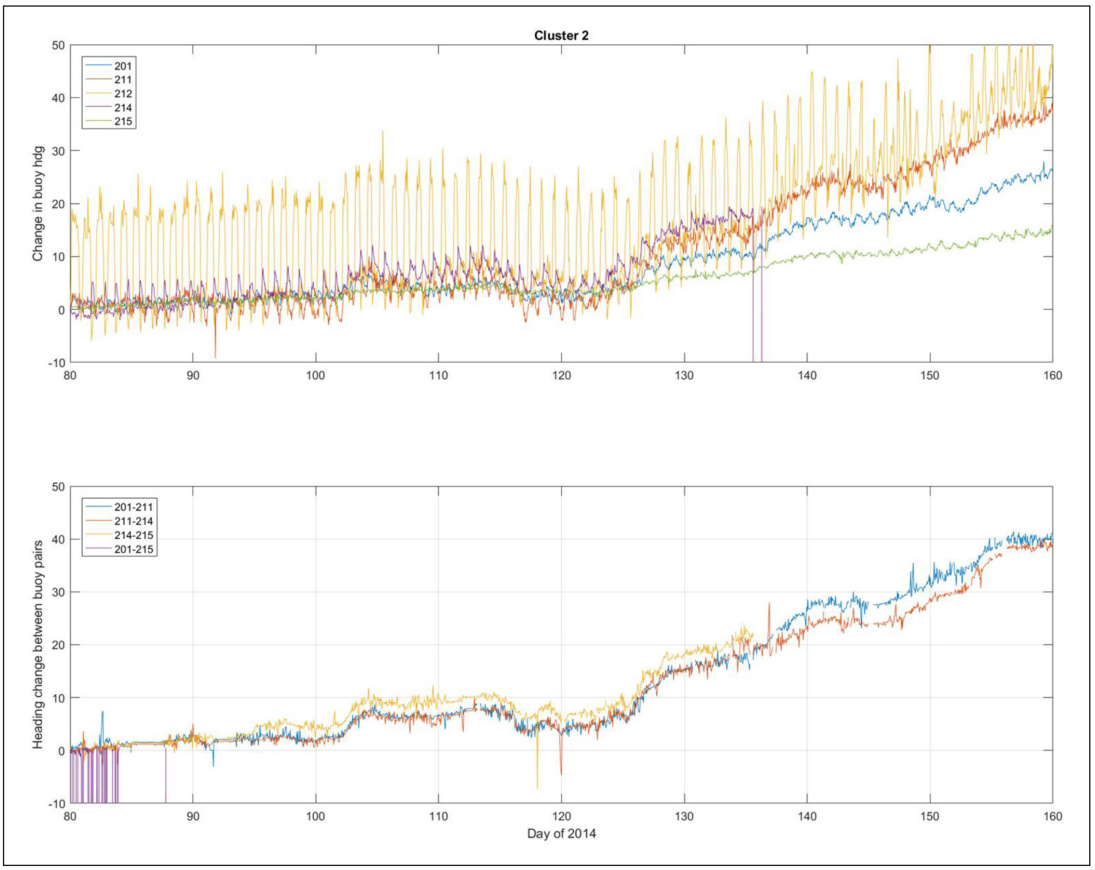

Figure 7: Comparison between changes in individual buoy heading and changes in bearing angle between buoy pairs. In this example, headings from buoys 211, 212 and 214 (top panel) closely track the bearing changes derived from GPS positions of the Cluster 2 buoys (bottom panel), reaching 40° variation by the end of the period. Buoys 201 and 215 headings vary much less, however, only reaching 25° and 15° change respectively. The match between individual buoy heading changes and the bearing changes indicates that the ice surrounding this cluster was rotating as an undeformed block. DOI: https://doi.org/10.1525/elementa.233.f7

The plot indicates that the previous tests were mostly able to correctly identify buoys with reliable and unreliable headings. Buoys are clearly indicated as bad if their headings remain very similar while the calculated solar azimuth changes significantly – buoys 213 (da = 195°) and 206 (da = 122°) show this behaviour, prefigured by their limited range of headings over their lifetimes. Other buoys that plot away from the equivalence line are 217 (da = 87°, three sun images) and 212 during three sun images captured at 1530: WB212 gives better solutions at 1830, however, with an overall da = 21°. WB202 plots well at the three 1530Z instances, but has –60° error for the four 0630 cases and +60° error at 1830, with a mean da = 55°.

Buoys that were believed to be suspect in previous tests but have robust results here are 201 (da = 15°, five sun images), 207 (da = 10°, six sun images) and 218 (da = 15°, five sun images). Other buoys are grouped close to the equivalence line, though seven of these have three-or-less sun images on which to base any evaluation, rendering the method less robust; none of these give obvious cause for concern.

3.4.5. Comparison with initial deployed orientations

As a final check, buoy headings (averaged in the component sense over three days immediately following deployment) are plotted in **Figure 9**. As previously mentioned, we aimed to deploy the buoys in a roughly south-facing orientation. Exceptions were 209 (facing West), 211 (facing North) and 212 (facing SE), which were constrained by topography to look towards their co-located IMBs. The plotted orientations appear broadly correct. The filled circles in **Figure 9** are coloured by the overall classification scheme of **Table 2.** These initial orientations broadly support this classification: WB206, 213 and 217 are clearly incorrect, as expected, though 202 appears well-oriented. All but one of the "maybes" also appear correct, with the exception of 215.

3.4.6. High frequency rotation

Headings were stored at one minute intervals, as the axisymmetric buoys were not expected to undergo rapid changes of orientation. To examine whether this was actually the case in practice, the angular heading change between minute samples was summed (positive clockwise, negative anticlockwise) to give a 'revolutions per file' value (RPF) for each 30-minute spectrum analysis period. While the quiescent period of the drifts showed RPF values predictably close to zero, the wave-influenced periods were commonly characterised by RPFs near two (*i.e.*, 720° rotation in 30 minutes). If uncompensated, such rotation would have serious impact on the quality of the directional wave spectrum calculation.

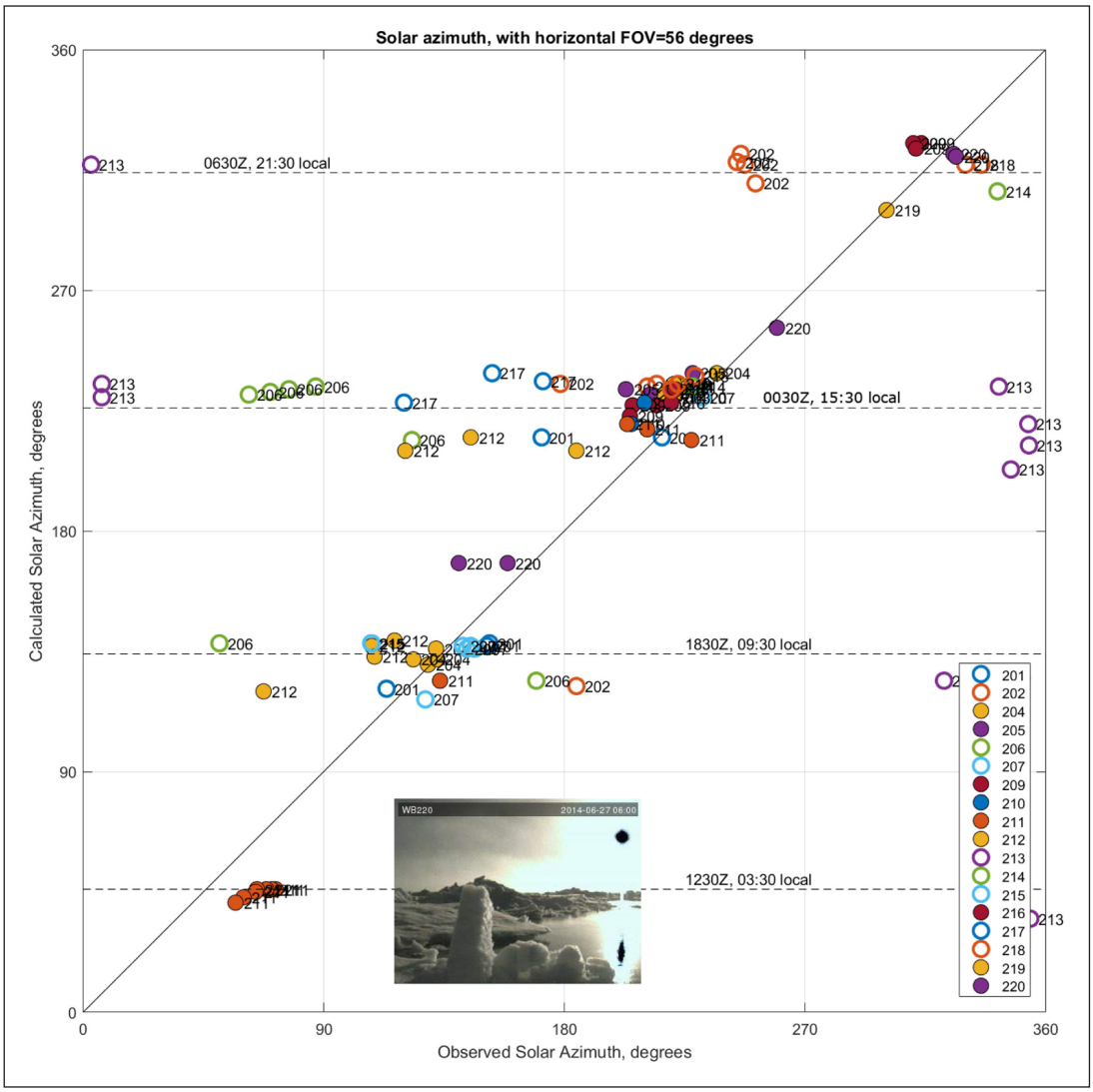

Figure 8: Observed solar azimuth in webcam images versus calculated value at that time and position. Filled circles indicate buoys that passed the heading-*versus*-bearing test and displayed the full 360° of heading variation during their lifetimes. Open circles indicate buoys which failed one or more of these tests. The diagonal line shows the 1:1 equivalence. Horizontal dashed lines indicate the approximate solar azimuth at the most common image times of 0030, 0630, 1230 and 1830 UTC, together with their local time equivalents. An example webcam image (inset) shows the obvious sun position (black disc). DOI: https://doi.org/10.1525/elementa.233.f8

Though variation between one-minute samples could be significant, they were at least progressive and allowed a cubic-spline interpolation to be used to calculate the heading (from *u*/v components) at each 1 Hz sample time. Buoy-referenced roll and pitch axes were then rotated into Earth co-ordinates on a sample-by-sample basis, prior to the directional wave spectrum calculation. Regressing the directional spread of calculated wave spectra against the corresponding RPF showed no correlation, indicating that any potential effect was well-compensated.

4. Discussion/conclusions

The deployment of 19 wavebuoy systems using fast-and-light air-supported ice camps from Sachs Harbour was very successful, though we must acknowledge the critical role of clear, flyable, weather conditions during the chosen week in mid-March. Once deployed, the buoys performed largely as hoped and proved suitably robust in the presence of waves in ice, despite the very imposing nature of the remnant ice cover as viewed in the webcam images.

The over-specified solar panels (60 W for a 4 W device) provided sufficient power for the buoys until the maximum daily sun angle dropped well below 20°, even during the almost-constant heavy cloud cover and nightly icing of the Arctic maritime autumn. The alkaline battery packs, used once solar power was exhausted, were apparently able to discharge almost their entire rated energy, with very little observed down-rating for the low temperatures. Twelve of the buoys survived until the exhaustion of these batteries. Four buoys likely succumbed to convergent ice dynamics/ridging, either being covered by piled up ice blocks or crushed, evidenced by webcam images and/or convergent local DKPs. The first buoy to fail (203) appears to have been struggling from the outset and likely had electronic problems leading to its early failure. The remaining two buoys (209 and 218) had no identifiable cause of early failure.

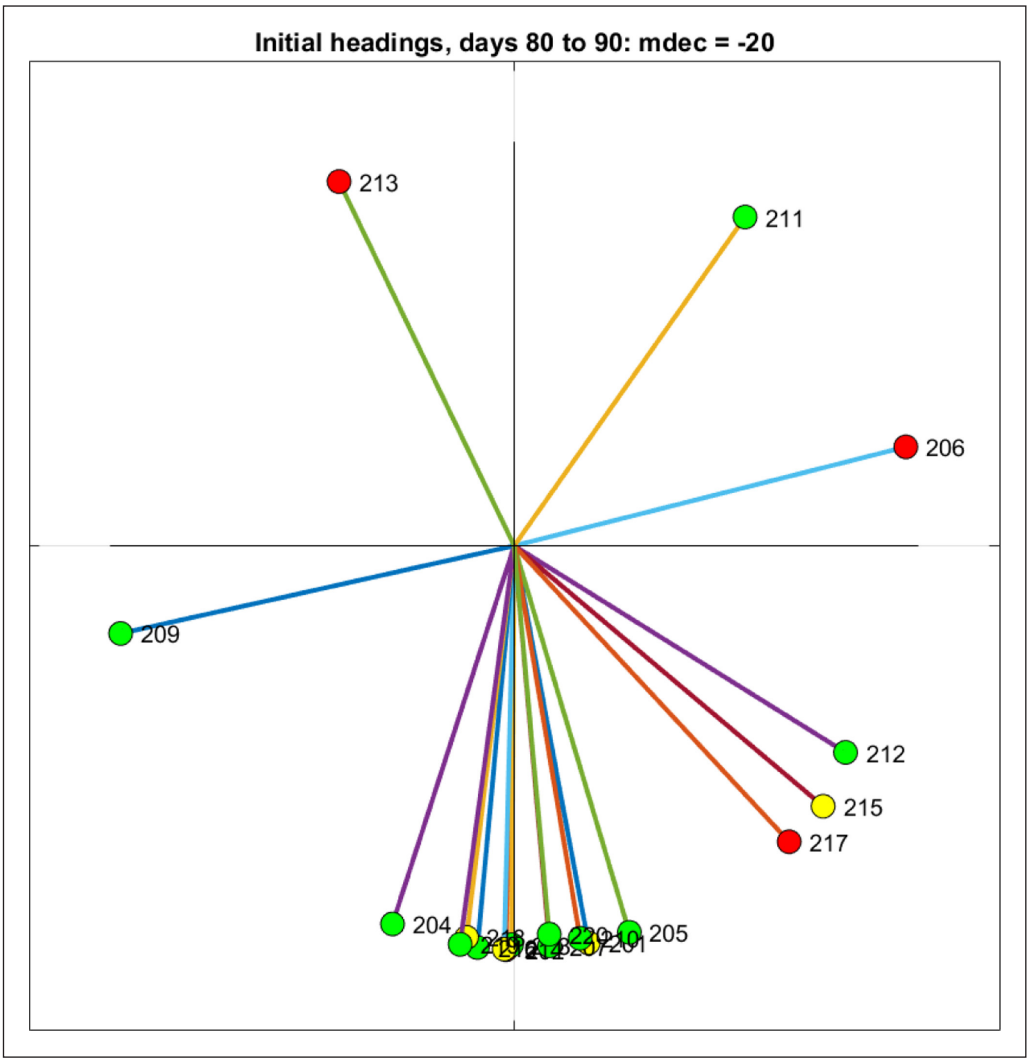

Figure 9: Initial headings for each buoy, averaged over the first three days of deployment when orientations were known. Filled circles are colour-coded by the classification scheme of Table 2, which this diagram largely supports: most buoys were oriented facing South, except 209 (West), 211 (NW) and 212 (SE). The buoys classified as 'bad' (206, 213, 217) have unexpected orientations here, though 202, also classified as 'bad', appears correct. Of the 'maybes', only 215 appears badly oriented in this plot. All headings are corrected to geographic north (True). DOI: https://doi.org/10.1525/elementa.233.f9

The throughput of the *Iridium* PPP system was sufficient to transmit six channels of continuous 1 Hz data from the 19 buoys, as well as hourly files of engineering and other parameters, though performance suffered towards the end of 2014 and perhaps contributed to the inability to re-establish contact with any buoys the following Spring. As mentioned, other *Iridium* users experienced similar problems over the same period, and switching to the *Iridium* RUDICS protocol (which was apparently unaffected) is now essential. Our custom two-way communication protocol showed its worth in allowing internal software failures in four of the GPS receivers to be corrected.

After an uneventful early drift, all buoys toppled onto their sides shortly after the quasi-simultaneous appearance of melt-ponding across the array and remained inclined at up to 70° until they were finally released to float upright, some two months later. For many of the buoys, the release coincided with the onset of significant waves, as they drifted in low-concentration (16 to 31%) ice bands, formed from fragments of the deformed ice cover that remained once the undeformed ice had largely melted away.

The quantification of heading accuracy was complicated by the limited availability of information for three of the methods presented here. Several buoys could not be reliably assessed by a single method, whether due to a subset of the buoys experiencing waves (comparison with WAM), the deformation of Cluster 3 prior to any significant whole-body rotation (heading *versus* bearing), or the lack of sufficient webcam images containing the solar disc (solar azimuth). Synthesising the results of all methods does give a clear picture of the magnetometer performance, and suspected shortfalls were generally confirmed across techniques. The comparison with WAM wave arrival direction appeared least useful: though the RMS differences measured by the 'failed' buoys were amongst the highest listed, the division between good and bad was far from clear in this test. Such are the problems of convolving noisy physics with noisy sensors.

It is clear that the SBG IG-500s used here are close to their practical magnetic field inclination limit. Eleven of the 19 buoys do give usable heading solutions nonetheless. Four buoys (201, 214, 215, 218) are likely compromised, though the final solar azimuth test gives more confidence in their results. Two buoys (202, 217) are sub-standard and two buoys (206, 213) give headings that are completely false. As we are confident that the magnetic calibration performed on the ice for each buoy was as similar as possible, such variation between buoys is unexplained, especially given the apparent concentration of poor performance in Cluster 3. Speculating about cluster-specific causes, rough handling during loading/unloading to/from the aircraft is the most plausible explanation. This supposition is reinforced by the fact that the fifth buoy in that cluster (208) failed even to boot-up on deployment, presumably due to a dislodged microSD card which holds the operating system. In retrospect it would have been very helpful to rotate each buoy slowly, pausing at the four cardinal points just after the system began logging, and we strongly recommend this procedure for future in-ice deployments if time allows.

The unexpectedly high rotation of the buoys during significant wave events makes a reliable heading solution crucial for deriving directional wave spectra, as each roll/pitch sample pair must be rotated into Earth coordinates prior to calculation of the directional moments. Though the roll and pitch axes are mutually orthogonal whatever the heading, any heading variation during the 30-minute sample period will cause the directional signal to be artificially smeared if not correctly compensated. The four buoys with unacceptable heading solutions must therefore be excluded from any directional analyses, though their heave spectra remain valid.

Otherwise, the quality of the directional wave data appears good, although effects of ice impact on the buoy hulls were seen and required careful quality control. The decision to transmit raw x/y/z accelerations in addition to the heave/roll/pitch outputs was well justified, as the 'black box' nature of the proprietary Kalman and anti-aliasing filters embedded in the AHRS would otherwise have obscured the nature (or perhaps existence) of such problems. While the advent of low-cost miniature AHRSs has been a boon to the development of wave measuring platforms, increased vigilance as to the veracity of the outputs is required.

Data Accessibility Statement

The following datasets were generated and will be included in the ONR MIZ project data repository once that is finalised. In the meantime, data are available on request from the Corresponding Author.

1. Directional wave spectra at 30-minute intervals, including GPS position.

Acknowledgements

We thank the many contributors to a successful deployment campaign in March 2014, including Great Slave Helicopters, Ken Borek Air, the British Antarctic Survey flight crew, the people of Sachs Harbour and the logistics team at the Applied Physics Laboratory, University of Washington. We also thank BAS technicians Scott Polfrey and Daniel Ashurst for their contribution to mechanical design and prototype build. Magnetic declination was calculated using the DMSP-MAG-1 model and Matlab routine provided by Patrick Alken at the Cooperative Institute for Research in Environmental Sciences (CIRES). Solar azimuth was calculated using a Matlab routine provided to the Matlab file exchange by Darin C. Koblick.

Funding information

The work formed part of the Office of Naval Research "Marginal Ice Zone" Departmental Research Initiative. Authors were supported by Grant Numbers N000141210130 (Wadhams and Doble), N000141210359 (Wilkinson, Maksym and Hwang).

Competing interests

The authors have no competing interests to declare.

Author contribution

- Substantial contributions to conception and design: MJD, JPW
- Acquisition of data: MJD, JPW, TM, LV, AT, JR, MP, PW
- Analysis and interpretation of data: MJD, BH, JRB, TM
- Drafting the article or revising it critically for important intellectual content: MJD, JPW, TM
- Final approval of the version to be published: MJD, JPW, LV, JRB, BH, TM, PW
- Note: Andrew Tait cannot give his approval as he is sadly recently deceased.

References

Alken, P, Redmon, RJ, Rich, FJ, Maus, S and **Luhr, H** 2013 Geomagnetic field modelling with DMSP. *AGU Fall Meeting, San Francisco,* abstract #GP53C-1158.

Doble, MJ and **Bidlot, JR** 2013 Wavebuoy measurements at the Antarctic sea ice edge compared with an enhanced ECMWF WAM: towards global waves-in-ice modelling. *Ocean Modelling*, **70**: 166–173, *Special Issue on ocean surface waves.* DOI: https://doi.org/10.1016/j.ocemod.2013.05.012

Elosegui, P, Wilkinson, J, Olsson, M, Rodwell, S, James, A, et al. 2012 High-precision GPS autonomous platforms for sea ice dynamics and physical oceanography, *Fall AGU Abs.* C13E-0662.

Hwang, B, Wilkinson, JP, Mayksm, E, Graber, HC, Schweiger, A, et al. 2017 Winter-to-summer transition of Arctic sea ice breakup and floe size distribution in the Beaufort Sea during 2014 ONR MIZ experiment. *Elem Sci Anth.* In press for INFLUX Special Feature.

Knepp, TN, Bottenheim, J, Carlsen, M, Carlson, D, Donohoue, D, et al. 2010 Development of an Autonomous Sea Ice Tethered Buoy for the Study of Ocean-Atmosphere-Sea Ice-Snow Pack Interactions: the O-buoy. *Atmos. Meas. Tech.* **3**: 249–261. DOI: https://doi.org/10.5194/amt-3-249-2010

Lee, CM, Cole, S, Doble, MJ, Freitag, L, Hwang, P, et al. 2012 Marginal Ice Zone (MIZ) program: science

and experiment plan. *Technical Report, APL-UW* 12-01, Applied Physics Laboratory, University of Washington.

Mei, CC 1989 *The Applied Dynamics of Ocean Surface Waves*. Advanced Series on Ocean Engineering, **1**: 768. World Scientific.

Thomson, J, Talbert, J, de Klerk, A, Brown, A, Schwendeman, M, et al. 2015 Biofouling effects on the response of a wave measurement buoy in deep water. *J. Atmos. Ocean. Tech*. DOI: https://doi.org/10.1175/JTECH-D-15-0029.1

Tucker, MJ 1991 *Waves in Ocean Engineering: Measurement, Analysis, Interpretation*, 431. Ellis Horwood, Chichester.

Valcic, L, Wilkinson, J, Doble, MJ, Maksym, TL and **Robst, J** 2014 Arctic Ocean Communications: Performance of High-Data Transmission Over The Iridium System. Poster C31D-0344, *AGU Fall Meeting*, San Francisco, December 2014.

Wadhams, P and **Doble, MJ** 2009 Sea ice thickness measurement using episodic infragravity waves from distant storms, *Cold Reg Sci. & Tech.* **56**: 98–101. DOI: https://doi.org/10.1016/j.coldregions.2008.12.002

Zippel, S and **Thomson, J** 2016 Air-sea interactions in the marginal ice zone. *Elem Sci Anth* **4**: 95. DOI: https://doi.org/10.12952/journal.elementa.000095

How to cite this article: Doble, MJ, Wilkinson, JP, Valcic, L, Robst, J, Tait, A, Preston, M, Bidlot, J-R, Hwang, B, Maksym, T and Wadhams, P 2017 Robust wavebuoys for the marginal ice zone: Experiences from a large persistent array in the Beaufort Sea. *Elem Sci Anth,* X(X): XX, DOI: https://doi.org/10.1525/elementa.233

Domain Editor-in-Chief: Jody W. Deming, University of Washington

Guest Editor: Craig Lee, University of Washington Applied Physics Laboratory

Knowledge Domain: Ocean Science

Part of an *Elementa* Special Feature: Marginal Ice Zone Processes in the Summertime Arctic

Submitted: 01 February 2017 **Accepted:** 17 June 2017 **Published:** XX Month 201X

ELEMENTA Science of the Anthropocene

Elem Sci Anth is a peer-reviewed open access journal published by University of California Press.

OPEN ACCESS

Typesetting queries

1. The following items have been included within the reference list, but are not cited within the text. For each un-cited reference, please advise where it should be cited in the text, or confirm that it can be removed from the reference list.
    a. Ref no. 6. " **Lee, CM, Cole, S, Doble, MJ, Freitag, L, Hwang, P,** et al. 2012 "